

Highly sensitive, ultra-low detection limit 3-D DNA nanostructure biosensor based on functionalized reflective optical fiber probe

Yufang Chen(陈彧芳), Wenbo Zhao(赵文博), Jinxing Xiong(熊金鑫), Jiashu Zhang(张家树), Kai Zhang(张开), Jiale Xie(解嘉乐), Menghan Liu(刘梦涵), and Hongdan Wan(万洪丹)
Citation: Chin. Phys. B, 2026, 35 (**5**): 054207. DOI: 10.1088/1674-1056/ae067f
http://cpb.iphy.ac.cn; http://iopscience.iop.org/cpb

What follows is a list of articles you may be interested in

Temperature and acoustic impedance simultaneous sensor based on forward stimulated Brillouin scattering in highly nonlinear fiber

Shilong Liu(刘仕龙), Yang Li(李阳), Hongbin Hu(胡洪彬), Bing Sun(孙兵), and Zuxing Zhang(张祖兴)
Chin. Phys. B, 2025, 34 (**7**): 074212. DOI: 10.1088/1674-1056/adca1b

Design of a high sensitivity and wide range angular rate sensor based on exceptional surface

Xinsheng Ding(丁鑫圣), Wenyao Liu(刘文耀), Shixian Wang(王师贤), Yu Tao(陶煜), Yanru Zhou(周彦汝), Yu Bai(白禹), Lai Liu(刘来), Enbo Xing(邢恩博), Jun Tang(唐军), and Jun Liu(刘俊)
Chin. Phys. B, 2024, 33 (**8**): 084204. DOI: 10.1088/1674-1056/ad4324

Multi-functional photonic spin Hall effect sensor controlled by phase transition

Jie Cheng(程杰), Rui-Zhao Li(李瑞昭), Cheng Cheng(程骋), Ya-Lin Zhang(张亚林), Sheng-Li Liu(刘胜利), and Peng Dong(董鹏)
Chin. Phys. B, 2024, 33 (**7**): 074203. DOI: 10.1088/1674-1056/ad3b85

Optical image encryption algorithm based on a new four-dimensional memristive hyperchaotic system and compressed sensing

Yang Du(都洋), Guoqiang Long(隆国强), Donghua Jiang(蒋东华), Xiuli Chai(柴秀丽), and Junhe Han(韩俊鹤)
Chin. Phys. B, 2023, 32 (**11**): 114203. DOI: 10.1088/1674-1056/acef08

Simultaneous measurements of refractive index and temperature based on a no-core fiber coated with Ag and PDMS films

Yuxin Li(李宇昕), Hailiang Chen(陈海良), Yingyue Zhang(张赢月), Qiang Chen(陈强), Biao Wu(武彪),Xiaoya Fan(樊晓亚), Yingchao Liu(刘英超), and Mingjian Ma(马明建)
Chin. Phys. B, 2023, 32 (**5**): 054209. DOI: 10.1088/1674-1056/ac8f36

Highly sensitive, ultra-low detection limit 3-D DNA nanostructure biosensor based on functionalized reflective optical fiber probe

Yufang Chen(陈彧芳)[1,†], Wenbo Zhao(赵文博)[2], Jinxing Xiong(熊金鑫)[2], Jiashu Zhang(张家树)[1], Kai Zhang(张开)[2], Jiale Xie(解嘉乐)[2], Menghan Liu(刘梦涵)[1], and Hongdan Wan(万洪丹)[2,‡]

[1] *School of Network and Communication, Nanjing Vocational College of Information Technology, Nanjing* 210023, *China*
[2] *Advanced Photonic Technology Laboratory, Nanjing University of Posts and Telecommunications, Nanjing* 210023, *China*

(Received 1 August 2025; revised manuscript received 3 September 2025; accepted manuscript online 15 September 2025)

A highly sensitive, ultra-low detection limit 3-D DNA nanostructure biosensor based on functionalized reflective optical fiber probe (ROFP) is proposed and demonstrated. Our approach achieves a mass limit of detection of ∼ 10 aM based on the ROFP. A particular single-nucleotide mismatch sequence is also identified. The sensitivity of the proposed DNA biosensor is 1.51 nm/lgaM, about three-fold higher than using single-strand DNA probes (0.47 nm/lgaM) and with high specificity. The proposed ROFP has high compactness (with a length of ∼ 3 mm) which is convenient for sample detection with small volume and complex gradients in small spaces with high sensitivity.

Keywords: DNA biosensor, ultra-low detection limit, high sensitivity, reflective optical fiber probe, secondary interference, 3-D DNA nanostructure

PACS: 42.81.–i, 42.81.Pa, 87.85.fk

DOI: 10.1088/1674-1056/ae067f **CSTR:** 32038.14.CPB.ae067f

1. Introduction

Viral infections are a primary cause of worldwide mortality, significantly endangering public health and safety.[1,2] The antibody and nucleic acid tests are mainly methods for virus detection. The effectiveness of antibody testing depends on the immune system initiating a response and the accuracy is low.[3] Especially, deoxyribonucleic acid (DNA) as the genetic material of most organisms, viruses and pathogens, stores essential genetic information for synthesizing RNA and proteins.[4,5] DNA biosensors, leveraging the specific identification and accurate quantitative assay of DNA sequences, can effectively discriminate among various organisms, thereby offering robust support for disease diagnosis.[6] The integration of polymerase chain reaction (PCR) technology with fluorescence represents the gold standard in contemporary field of nucleic acid detection.[7] However, the false negatives and time cost are relatively high due to the labeling process. Furthermore, enhancements are needed in sensitivity, limit of detection (LoD), and specificity.[8] Developing a label-free, ultrasensitive, real-time DNA detection method with low LoD continues to be a significant challenge.

Due to the strong evanescent fields, simple preparation processes, and low cost, optical fiber biosensors (OFBs) have rapidly emerged in applications of medicine and biology in recent years, especially in building diagnostic platforms for rapid and accurate detection of viral diseases.[9,10]

Recently, a range of label-free DNA OFBs crafted with diverse structures have emerged,[11–15] all of which are characterized by biocompatibility, versatility in function, ability to operate in real time, as well as low LoD and high sensitivity. Wu *et al.* proposed a AuNPs-DNA conjugate aptamer OFB for cortisol detection, with sensitivity of 0.11 (a.u.)/nM and LoD of 1 nM.[11] Lang *et al.* proposed a metabolite OFB based on AuNPs and MXene quantum dots modified taper-in-taper single-mode fiber (SMF), with sensitivity of 1.93 nm/mM and LoD of 146.11 μM.[12] Delgado *et al.* proposed a DNA OFB utilizing long period grating, with sensitivity of 0.25 nm/μM and LoD of 10 nM.[13] Li *et al.* proposed an alpha-fetoprotein OFB based on multimode fiber (MMF)-multicore fiber (MCF)-MMF, with sensitivity of 1.32 nm/lg(ng/mL) and LoD of 84 pg/mL.[14] Recently, we proposed a tapered thin-diameter photonic crystal fiber interferometer (TTD-PCFI) OFB for DNA detection, with sensitivity of 632 pm/lg(fM) and LoD of 410 aM.[15]

Most reported straight-through structure OFBs lack flexibility and system integration, limiting the interaction strength between the optic field and biomolecules. OFBs based on the reflective probe structures can penetrate certain biological sample solution in narrow and semi-enclosed space.[16–21] Cao *et al.* proposed a high sensitivity OFB probe of SMF-tapered four core-SMF, with LoD of 4.35 pg/mL.[16] Gong *et al.* proposed a multimode plastic-clad silica probe modified by gold film for DNA hybridization, with sensitivity of 0.13 nm/nM and LoD of 4.9 nM.[17] Wen *et al.* proposed a label-free DNA OFB using U-shaped probe, with sensitiv-

†Corresponding author. E-mail: chenyf@njcit.cn
‡Corresponding author. E-mail: hdwan@njupt.edu.cn

© 2026 Chinese Physical Society and IOP Publishing Ltd. All rights, including for text and data mining, AI training, and similar technologies, are reserved.

ity of −218.32 nm/(ng/mL) and LoD of 0.01 ng/mL.[18] Li *et al*. proposed a label-free DNA OFB based on a reflective microfiber probe, with a low LoD of 10 pM.[19] Li *et al*. proposed a MMF-SMF probe DNA sensor modified by metal-organic frameworks, with sensitivity of −7.72 nm/lg(μM) and LoD of 3 pM.[20] Ran *et al*. proposed a hypoxia-sensitive fluorescent fiber probe to realize fast and accurate tumor recognition and diagnosis, the limit of quantification is ∼ 5 ng/mL.[21] Recently, Li *et al*. presented ultrasensitive and ultra-low detection of exosomes, prostate specific antigen and carbonic anhydrase IX protein based on strong plasmonic effect of a microfiber probe, with LoDs of 3.97 fM, 9.32 particles/mL and 13.8 zM.[22–24]

However, biosensing interfaces of above OFBs are pure quartz fiber or metallic material, with single-stranded DNA (ssDNA) probes modified onto the sensing interface to capture target DNA molecules.[25] The existence of electrostatic repulsion, conformational instability, lodging, entanglement, stacking, and disordered aggregation, resulting in non-specific adsorption, reduced recognition efficiency and speed, ultimately limiting the sensitivity, LoD, and specificity. Constructing a highly sensitive biological sensor interface is expected to further enhance high-efficiency binding between DNA molecules.[26–28]

In this paper, a highly sensitive, ultra-low detection limit 3-D DNA nanostructure biosensor based on functionalized reflective optical fiber probe (ROFP) is proposed and demonstrated. The proposed ROFP is fabricated by flame heating, drawing method, with a stress vertical fractured reflection end-face, which enhances the transmission length and intensity of evanescent field due to the secondary interference. The ROFP is functionalized by 3-D tetrahedral DNA nanostructure (TDN) probes to further enhance the sensing performance for label-free DNA detection, with a high sensitivity of 1.51 nm/lgaM ranged from 10 aM to 100 fM and an ultra-low LoD of ∼ 10 aM. Sequence with a single-nucleotide mismatch is also identified. The proposed DNA nanostructure biosensor exhibits exceptional performance in terms of label-free, excellent specificity, high sensitivity and ultra-low LoD, rendering it a highly favorable utilization in vitro detection, drug delivery, gene diagnosis, protein identification, and environmental monitoring.

2. Theoretical analysis and fabrication

2.1. Theoretical analysis

Figure 1(a) shows the schematic diagram of the ROFP, including two ports (port 1 and port 2), a coupling region (sensing area) and a reflection tip. L is the coupling length, D is the waist diameter of ROFP. According to the supermodes theory, when light enters through port 1 and arrives at the coupling region, both the two supermodes (even and odd) are excited and propagate towards the end-face. Then the two supermodes are reflected again to the ROFP's coupling region and generate secondary interference. An envelope interference spectrum is formed at port 2. Figures 1(b) and 1(c) are the comparison results of simulated interference intensity distribution along the ROFP within coupling region by using the beam propagation method (BPM). The operation wavelength is 1550 nm and the surrounding refractive indices (RIs) are 1 and 1.3333, respectively. D is ∼ 6 μm and L is ∼ 3 mm. It can be seen that when the ROFP is immersed in aqueous solution (RI = 1.3333) from air (RI = 1), the power exchange changes drastically and the evanescent field leakages increase within coupling region of the ROFP. Due to the secondary interference, the ROFP enhances the length and intensity of evanescent field. The transmission power between the two micro-nano fibers in the coupling region is exchanged between each other, resulting in variations of the output power and reflection spectrum at port 2.

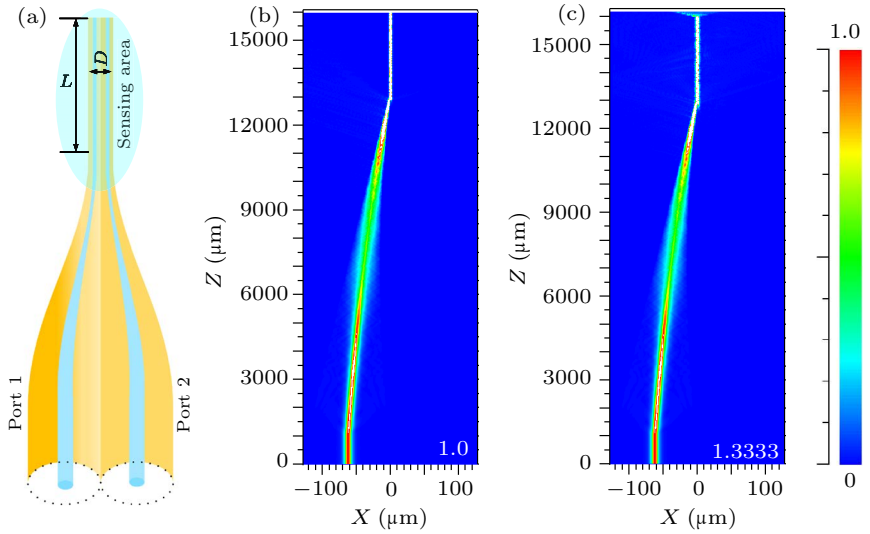


Fig. 1. Simulation analysis. (a) Schematic diagram of the ROFP. (b) and (c) Interference intensity distribution along the ROFP within coupling region in the RIs of 1.0 and 1.3333, respectively.

The output of the ROFP presents the power coupling and exchange due to the interference between supermodes in the whole coupling region. The ROFP is weakly coupling and the coupling coefficients C (C_x: x polarization; C_y: y polarization) are expressed as[29]

$$C_{x/y} = \frac{2^{3/2}(n_1^2 - n_0^2)^{1/2} U_\infty^2 (2n_1^2 V + 1)}{n_1^3 a(\sqrt{\pi}) V^{7/2}}, \tag{1}$$

where n_1 and n_0 denote the RIs of silica and air, $a = D/2$, $U_\infty = 2.405$ and $V = [(2\pi a)/\lambda](n_1^2 - n_0^2)^{1/2}$. When light enters the input port 1 and reflected by the tip, the power emerging from port 2 is

$$P_2 = \frac{1}{2}\left(\frac{n_1 - n_0}{n_1 + n_0}\right)^2 \left\{1 - \cos[(\bar{C}_x + \bar{C}_y)L]\cos[(\bar{C}_x - \bar{C}_y)L]\right\}, \tag{2}$$

where $\bar{C}_x$ and $\bar{C}_y$ are the averaged values over the whole coupling region.

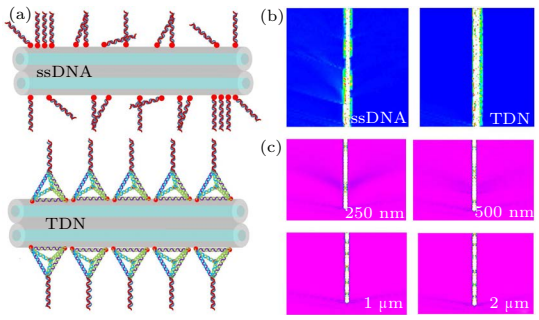


Fig. 2. Interaction between evanescent field and DNA biomolecules based on ROFP. (a) Spatial conformation of two DNA probes. (b) Simulated intensity distribution between evanescent field and different biomolecular layers. (c) Interference intensity with different thicknesses of DNA probe's medium layer.

Figure 2(a) shows the different spatial conformations of the TDN and ssDNA probes on ROFP's surface, resulting in different DNA combination mechanisms. ssDNA probes undergo lodging, inter strand entanglement, tight packing and inclined to lie flat, whereas 3-D TDN probes feature an attractive functional scaffold that confers rigidity and stability. This design effectively suppresses non-specific binding, improves sensitivity, lowers detection limits, expands dynamic ranges and accelerates reaction kinetics.[30] Figure 2(b) is the simulated interference intensity distribution between evanescent and different biomolecular layer along the ROFP functionalized by ssDNA and TDN probes. Obviously, the TDN probes exhibit greater mechanical rigidity and structural stability than the ssDNA probes, achieving more uniform intensity distribution, higher DNA hybridization efficiency and stronger field-material interactions. Figure 2(c) is the interference intensity distribution of ROFP's strong coupling region with different thickness of DNA probe's medium layer. As the thickness is increased from 250 nm to 2 μm, the mode-field interference forms a distinct "serpentine" distribution, enhancing the interaction between the evanescent field and DNA biomolecules.

2.2. Fabrication

The proposed ROFP is fabricated through flame heating and drawing method, with a vertical cut in the waist region to create a Fresnel reflective end-face. Firstly, two parallel aligned SMFs (the cladding/core diameters of 125 μm/8.2 μm) are adiabatically tapered and weakly fused together to form an optic fiber micro-coupler (OFMC). Then heating is stopped and an axial tension is exerted on the fibers. Then, due to the brittle fracture of the silica fiber, the waist region of the OFMC is snapped under vertical stress to fabricate the ROFP with high Fresnel reflection end-face. Figures 3(a) and 3(b) show the microscopic photographs of the ROFP within the waist longitudinal section and transverse region, L is ~ 3 mm and D is ~ 6 μm, respectively.

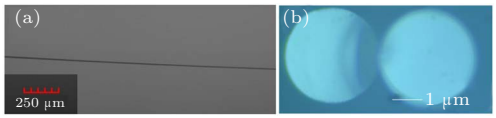


Fig. 3. Microscopic photographs of the fabricated ROFP: (a) longitudinal section, (b) transverse region.

3. Materials and surface functionalization method

In this experiment, piranha solution (Sigma, mixed with 3 vol of 98% H_2SO_4 and 1 vol of 30% H_2O_2) and poly-L-lysine solution (Sigma, PLL, 0.1% w/v in PBS buffer) as solvents are used for ROFP's surface functionalization.

Table 1. Sequences of DNA for synthetic TDN.

Oligonucleotide	5'End	Sequence (5'-3')	3'End
Tetra-A	none	CATCTTGCCTAAAAAAAAAAACATTCCTA AGTCTGAAACATTACAGCTTGCTACACGA GAAGAGCCGCCATAGTA	none
Tetra-B	NH_2–C6–	TATCACCAGGCAGTTGACAGTGTAGCAAG CTGTAATAGATGCGAGGGTCCAATAC	none
Tetra-C	NH_2–C6–	TCAACTGCCTGGTGATAAAACGACACTAC GTGGGAATCTACTATGGCGGCTCTTC	none
Tetra-D	NH_2–C6–	TTCAGACTTAGGAATGTGCTTCCCACGTAG TGTCGTTTGTATTGGACCCTCGCAT	none
Cy3-cDNA-target	none	TTTTTTTTTTAGGCAAGATG	Cy3–
ssDNA probe	none	CATCTTGCCTAAAAAAAAAA	NH_2–C6–
cDNA-target	none	TTTTTTTTTTAGGCAAGATG	none
1-ncDNA	none	TTTTTTTTTTATGCAAGATG	none

The oligonucleotides were purchased from Sangon Biotech (Shanghai) Co., Ltd. The specific base sequence information is listed in Table 1. For the purpose of mismatch identification, the target DNA, complementary DNA (cDNA) and non-complementary DNA (ncDNA) sequences are modified as follows, and underlined indicates the mismatched nucleotide.

3.1. Synthesis of TDN probe

Figure 4(a) shows the synthesis procedure of the TDN probe, dissolving 75-nucleotides of Tetra-A and three single-stranded Tetra-B, Tetra-C, and Tetra-D, each containing 55-nucleotides are modified with amino in ultrapure water at equimolar concentration. Then, mixed with TM buffer and oscillated slightly to form a final concentration of 1 μM. Subsequently, the mixture was subjected to denaturation at 95 °C for 10 min, rapidly cooled to 4 °C within 30 s and then incubated for 30 min using a thermal cycler to obtain TDN probe. Each edge of the self-assembled TDN probe contains 17-base pairs, the edge length and height are calculated to ∼ 5.8 nm and 4.74 nm, respectively. The gel electrophoresis in Fig. 4(b) demonstrates the effectiveness of the TDN probe synthesis, with a success rate > 95%.

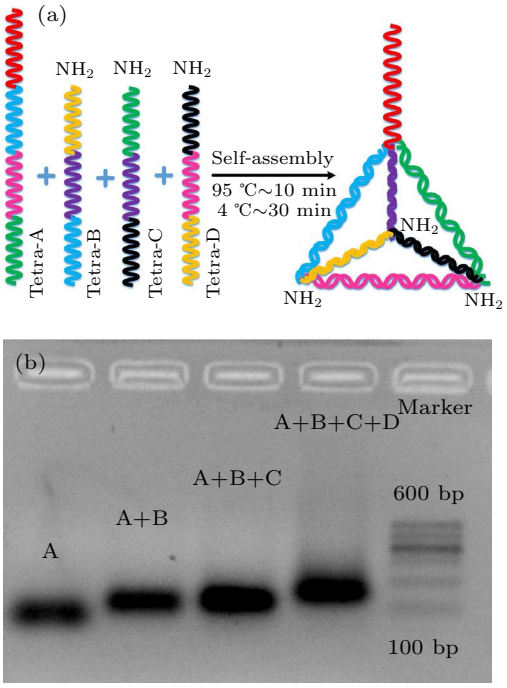


Fig. 4. Synthesis procedure of the TDN probe. (a) Synthesis procedure. (b) Assessment of synthesis efficiency.

3.2. Surface functionalization of ROFP

Owing to the reduced negative charge density on the surfaces of ROFP, the TDN probes could not bind to the SiO_2 ROFP's surface directly. Surface functionalization and modification of ROFP through physical adsorption and chemical bonding to achieve connection with the TDN probe is essential, which is shown in Fig. 5(a). Initially, the piranha solution is delivered into the polytetrafluoroethylene (PTFE) microfluidic channel for a duration of 30 min to trigger the activation of negatively charged hydroxyl groups on ROFP's surface. Then, the ROFP is immersed in PLL solution for 1 h. Finally, inject the TDN probe solution@1 μM into and stand for 1 h. The self-assembly of the TDN probes onto the functionalized ROFP's interface was achieved through covalent conjunction between the negatively charged probes and the amino of PLL, resulting in hydrazone bond –NH–NH–. Throughout the protocol of the functionalized ROFP, which is rinsed with ultrapure water for 10 min prior to each reagent exchange to eliminate residual contaminants (clean 1–4). Figure 5(b) reveals the measured reflection spectra of ROFP throughout the experimental functionalization process. Significant wavelength drift attributed to light–matter interactions within sequentially applied reagents, confirms successful surface functionalization via electrostatic adsorption and covalent grafting.

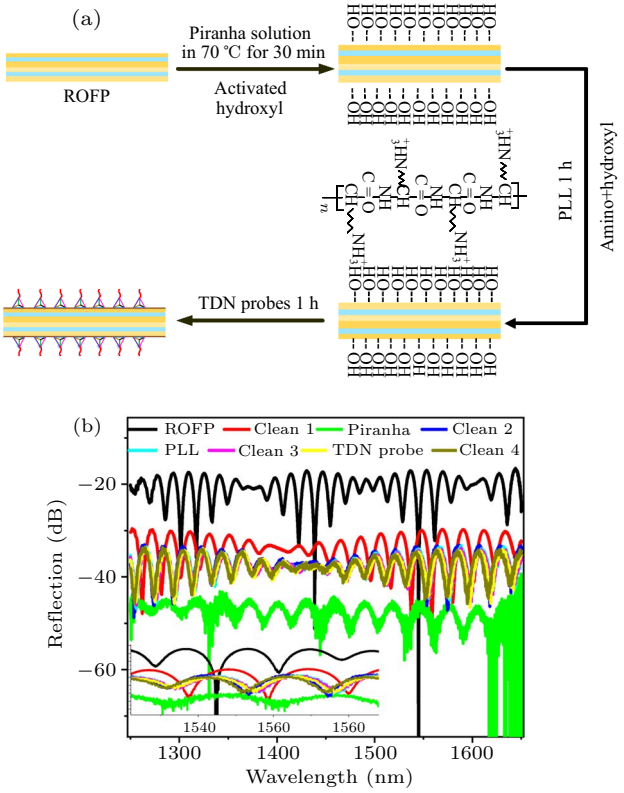


Fig. 5. ROFP's surface functionalization. (a) Protocol. (b) Measured reflection spectra in different biological liquid samples.

3.3. Fluorescence characterization of TDN and ssDNA probes

Figure 6 illustrates comparison and the ability of unfunctionalized versus functionalized ROFP to capture TDN or ssDNA probes and hybridize with target DNA. Fluorescence imaging is performed using a laser scanning confocal fluorescence microscope (FV1000MPE). The sample is excited with 517 nm and emissions are recorded through a tunable detector spanning 530 nm–630 nm. The TDN and ssDNA probes

are mixed with Cy3-labeled target ssDNA (Cy3-cDNA-target in Table 1) with equimolar volume. Following injection of the mixed solution into the ROFP and 1 h dark incubation, the TDN probe exhibits significantly enhanced fluorescence signal intensity and more homogeneous spatial distribution compared to the ssDNA probe based on the functionalized ROFP, as shown in Figs. 6(b) and 6(d). The specific morphology of the 3-D TDN probes is characterized by atomic force microscopy (AFM).[31] Furthermore, the ability of the unfunctionalized ROFP to anchor capture TDN and ssDNA probes was also investigated and compared in Figs. 6(a) and 6(c). The fluorescent signal distribution on the surface of the unfunctionalized ROFP is weak as compared to the functionalized ROFP. Thus, the proposed functionalization method of surface in conjunction with TDN probes demonstrates effective enhancement of molecular binding efficiency, accompanied by mitigation of probes' stacking and winding effect, which further enhances the sensitivity of the proposed DNA biosensor and reduce LoD.

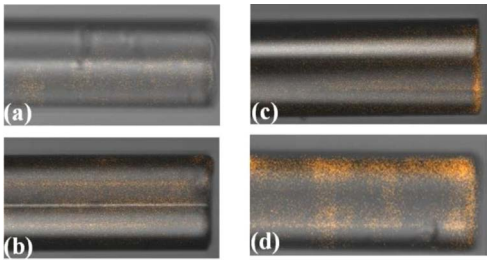


Fig. 6. The microscopic fluorescence images of ssDNA probes on (a) unfunctionalized ROFP, (b) functionalized ROFP; TDN probes on (c) unfunctionalized ROFP, (d) functionalized ROFP.

4. Experimental setup and results

4.1. Experimental setup

The experimental setup for DNA hybridization detection is illustrated in Fig. 7, comprises a broadband source (BBS, wavelength: 1250 nm–1650 nm), an optical spectrum analyzer (OSA, resolution: 0.02 nm), peristaltic pump (TJ-3A, minimum flow rate: 7 μL/min) and a PTFE microfluidic channel. The ROFP is integrated into the PTFE microfluidic channel, enabling automated syringe pump mediated injection and withdrawal of the test solutions. Port 1 of the ROFP is connected to the BBS and the output reflection spectrum is measured by OSA through port 2, monitoring the interactions of the ROFP in real time with different reagents. The microfluidic channel is placed in a thermally- and vibration-isolated container in a constant temperature environment. A minimum flow rate setting eliminates flow related and frictional interferences for accurate results.

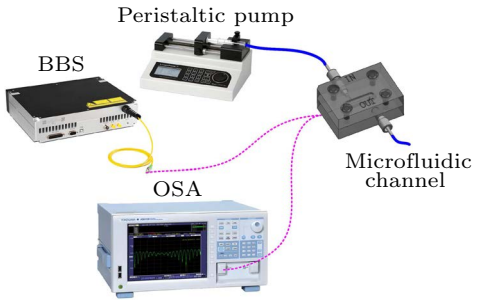


Fig. 7. Experimental setup for DNA hybridization detection based on the ROFP.

4.2. RI sensing and stability

The measured reflection spectral shifts of the ROFP with different RI solutions (NaCl solutions, RI range: 1.3333–1.3639, $\Delta RI = 0.0051$) are monitored in real time. The changes in the surroundings of the ROFP lead to a dramatic spectral wavelength red-shift as the RI increases, as shown in Fig. 8(a). Figure 8(b) shows the relationship between the measured wavelength and RIs. The RI sensitivities are 5837.33 nm/RIU and 6129.05 nm/RIU around 1400 nm and 1500 nm, respectively.

Figure 9 shows the stability of the fabricated OFB based on ROFP in liquid. Figure 9(a) shows the measured reflection spectral response measured over 1 h, with magnified views highlighting the dips around 1295 nm and 1583 nm. Figure 9(b) depicts the corresponding fluctuations of wavelength, with $\Delta\lambda$s (wavelength shifts) falling within ± 0.2 nm and $\Delta\delta$s (standard deviation) remaining $< \pm 0.05$ nm.

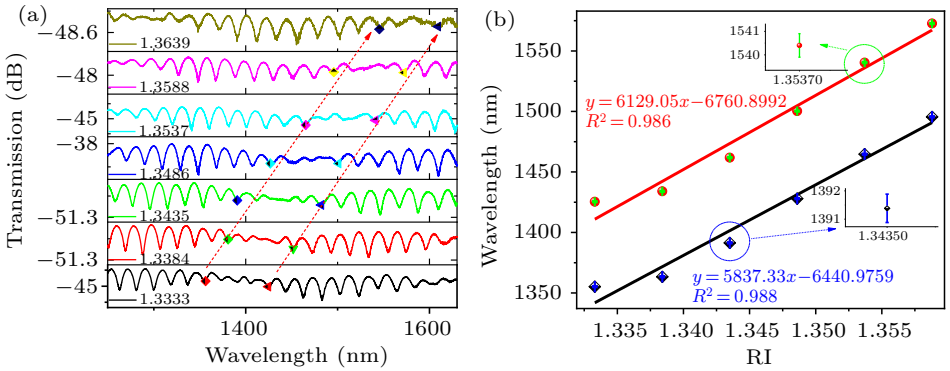


Fig. 8. Measured reflection spectra versus different RIs. (a) The reflection spectra. (b) The relationship between wavelength shift and RIs.

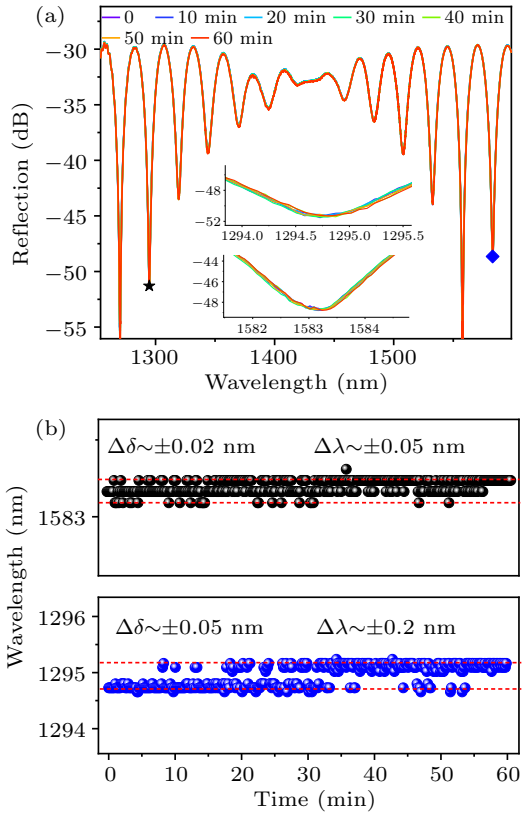


Fig. 9. Measured stability of the ROFP for 1 h. (a) Measured reflection spectra. (b) Wavelength fluctuations@1294 nm and 1583 nm.

4.3. Detection of DNA hybridization using TDN probe

The concentration of the 5'-amine functionalized TDN probe is 1 μM. The target ssDNA (cDNA-target in Table 1) solution is diluted with ultrapure water to five different concentrations (10 aM to 100 fM). The fabricated target ssDNA solutions are injected into the microchannel to react with the functionalized ROFP gradually, and rinsed by ultrapure water during each solution replacement. Figure 10(a) is the measured reflection spectra in target ssDNA solutions. As the concentration of target ssDNA is increased from 10 aM to 100 fM, the reflection spectra of ROFP red-shift. Figure 10(b) shows the real-time evolution of wavelength shifts in the presence of varying target ssDNA solutions. At the initial stage, the wavelength shifts change dramatically, followed by a tendency toward stabilization. The reaction proceeds rapidly and each concentration level demonstrates a distinct jump step at the starting point. Due to the adjustable size of the 3-D TDN probes and compact structure of the ROFP, the measured response time of the proposed biosensor can be reduced to 10–15 min. The inset is the relationship between wavelength shift and target DNA's concentration, with a high sensitivity of 1.51 nm/lgaM and $R^2 = 0.97$. For the target DNA solution@10 aM, the wavelength shift is measured to be ~ 2.9 nm, which is much higher than the wavelength shift of the blank sample ultrapure water (0.02 nm). The wavelength shift will remain stable as the DNA concentration continues to increase, and the detectable concentration is 10 aM at least (LoD < 10 aM).

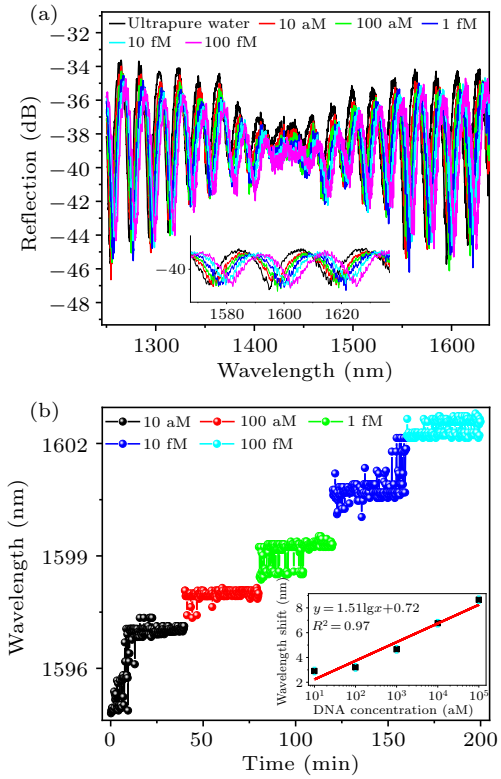


Fig. 10. Measurement of DNA hybridization. (a) Wavelength red-shift with increased concentration. (b) Corresponding wavelength shifts versus time. The inset: the relationship between wavelength shift and concentration.

4.4. Specificity detection using TDN probe

Non-complementary and target ssDNA solution was employed to assess the specificity for the DNA hybridization

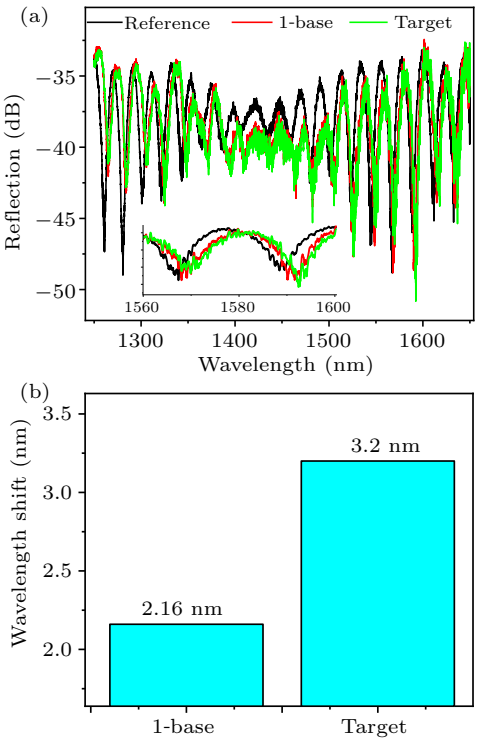


Fig. 11. Measured specificity. (a) Experimentally measured spectra of matched and mismatched DNA solutions. (b) The detail wavelength shift of 1-base mismatch and target ssDNA.

process. The concentration of target DNA is 10 fM. The measured response of specific recognition is shown in Fig. 11. Figure 11(a) shows the spectral wavelength shifts when different target DNAs are hybridized with the TDN probes, which are reference (blank sample), 1-base mismatch (1-ncDNA in Table 1, 1-base) and target ssDNA (target). The inset is the details of the spectral shift. Figure 11(b) shows the detailed wavelength shift of 1-base mismatch and target ssDNA. Comparing the shift of the target ssDNA ($\sim$ 3.2 nm), both the reference (0.02 nm) and 1-base mismatch induced drift (2.16 nm) are significantly smaller.

4.5. Detection DNA hybridization using ssDNA probe

For comparison, DNA hybridization using ssDNA probe is also measured, including the sensitivity and specificity. The ssDNA sequences are modified as follows, and the mismatched nucleotide is underlined in Table 2.

Table 2. Different ssDNA sequences.

Oligonucleotide		5'End	Sequence	3'End
Number of bases	probe ssDNA	none	CTACAGCGATACTGTGACGATCGTA	$-NH_2$
	target ssDNA	none	TACGATCGTCACAGTATCGCTGTAG	none
	1-base mismatch ssDNA	none	TACGATCGTCACAGCATCGCTGTAG	none
	2-base mismatch ssDNA	none	TACGATCGACACAGCATCGCTGTAG	none
	9-base mismatch ssDNA	none	TTCGCTCGACCCGGCATAGCTTTCG	none

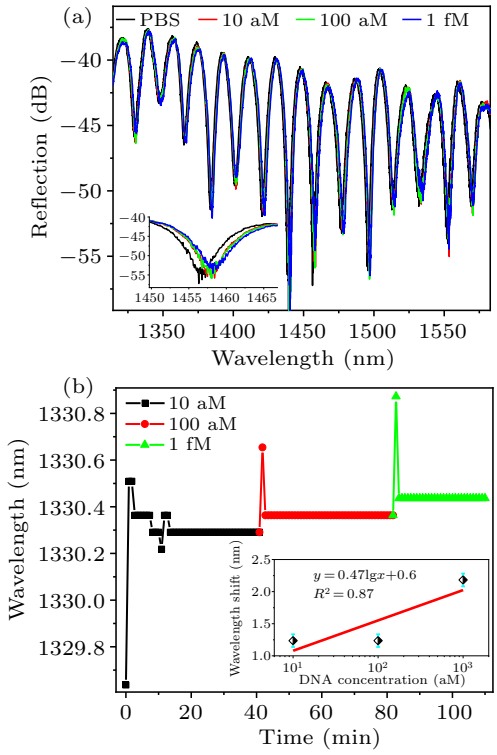


Fig. 12. Measured DNA hybridization detection using ssDNA probes. (a) The wavelength rightward shift with increased target ssDNA's concentration. (b) The wavelength shifts of different target ssDNA solutions versus time. The inset: the fitting curves of the relationship between wavelength shift and concentration.

The target ssDNA solution is diluted in 10$\times$ phosphate buffered saline (PBS) to prepare the different concentrations from 10 aM to 1 fM. The concentration of the ssDNA probe is 10 μM, which is higher than the TDN probe (1 μM). The reflection spectral wavelength exhibits a significant rightward shift as the target ssDNA concentration is increased from 10 aM to 1 fM, as shown in Fig. 12(a). For the target ssDNA solutions with concentrations of 10 aM, 100 aM, and 1 fM, the wavelength shifts are 0.65 nm, 0.72 nm, and 0.8 nm, respectively. Compared to the sensing performance using TDN probes, the wavelength shift of the ROFP using ssDNA probe is about six-fold lower (the wavelength shift based on TDN probe is $\sim$ 4.65 nm at 1 fM). Figure 12(b) depicts the real-time evolution of corresponding wavelength shifts and the inset shows the relationship between wavelength shift and target ssDNA's concentration, with sensitivity of 0.47 nm/lgaM and the lowest detectable concentration of at least 10 aM. The sensitivity of the proposed ssDNA biosensor is about three-fold lower than using TDN probes.

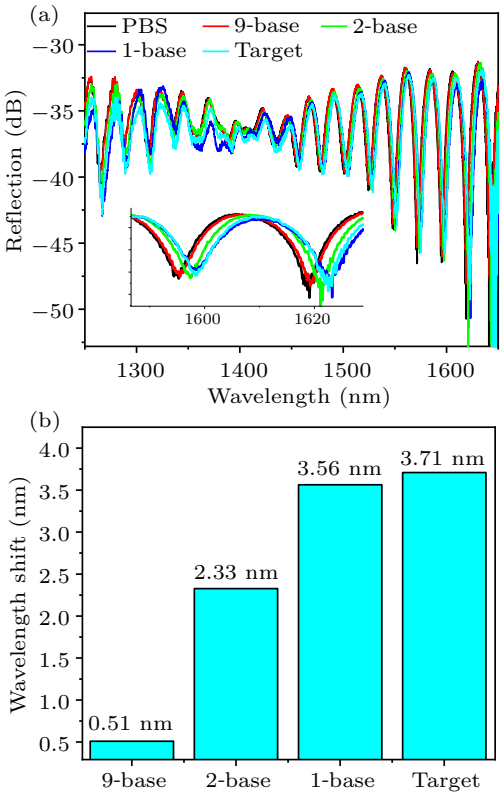


Fig. 13. Measured specificity. (a) Experimentally measured spectra of matched and mismatched DNA solutions. (b) Details of the spectral shift.

The measured spectral shifts for different target ssDNA,

which are 9-base mismatch (9-base), 2-base mismatch (2-base), 1-base mismatch (1-base) and target ssDNA (target) as shown in Fig. 13(a). Figure 13(b) shows that the spectral shifts of 9-base, 2-base and 1-base mismatch ssDNA are 0.51 nm, 2.33 nm, and 3.56 nm, respectively. The measured wavelength response of the target ssDNA is 3.71 nm, which is higher than that of 1-base mismatch target ssDNA. Thus, the single nucleotide mismatch recognition can be achieved. The proposed ROFP can specifically recognize the target ssDNA sequence. The drift difference between target ssDNA and 1-base mismatch target ssDNA is 0.15 nm, which is much lower than that of using TDN probes (1.04 nm). From the comparison between the measured results of ssDNA and TDN probes, the specificity of ROFP based on ssDNA probe is one order of magnitude lower than that of TDN probes. The detection of the proposed DNA OFB based on TDN probes has higher sensitivity and lower LoD.

As shown in Table 3, the proposed DNA biosensor is compared with OFBs based on different fiber-optic structures, including sensitivity (S), and LoD. It can be seen that the proposed DNA biosensor can achieve the highest sensitivity and lowest LoD for DNA detection. Currently, in order to further improve the LoD and sensitivity of OFBs: 1) Introducing optical device with high resolution and further improve the isolation of the biosensor. 2) Strengthening the interaction between evanescent field and matter, i) Optimizing the size of biosensor, enhancing the intensity and effective length between the evanescent field; ii) Using two-dimensional and metal materials to enhance the interaction of light-substance; iii) Exploring novel biosensing mechanisms, such as paritytime-symmetry[32] and kovacs-like memory effect.[33] 3) Regulating different nanostructured recognition probes to enhance the high density and high efficiency binding ability.

Table 3. Comparison performance between different DNA OFBs.

Structure	S	LoD	Ref.
Long period grating	0.25 nm/μM	10 nM	[13]
TTD-PCFI	632 pm/lg(fM)	410 aM	[15]
MMF-SMF	–7.72 nm/lgμM	3 pM	[19]
WGM resonator	4.95 pm/lgfM	10 pM	[34]
Tapered fiber	1.22 nm/lgM	1 fM	[35]
PCF	0.02 nm/nM	10 nM	[36]
C-type fiber	0.11 nm/nM	7.9 nM	[37]
MMF-NCF-MMF	0.41 nm/nM	1.39 nM	[38]
ROFP	1.51 nm/lgaM	10 aM	this work

5. Conclusion

In conclusion, a highly sensitive, ultra-low detection limit 3-D DNA nanostructure biosensor based on functionalized ROFP is proposed and demonstrated. The proposed ROFP is fabricated by flame heating and drawing method, with stress vertical fractured reflection end-face and enhanced length and intensity of evanescent field, due to the secondary interference, with a diameter of 6 μm and a sensing area of ∼ 3 mm. The ROFP's sensing interface is functionalized by TDN probes, which reduces the ssDNA probes' stacking and winding effect. Our approach achieves a mass limit of detection of ∼ 10 aM based on the proposed DNA OFB with a sensitivity of 1.51 nm/lgaM. Compared to the sensing performance using ssDNA probes, the wavelength shift of TDN probe (∼ 4.65 nm@1 fM) is about six-fold higher than that using ssDNA probe (∼ 0.8 nm@1 fM). A particular single-nucleotide mismatch sequence is also identified. The specific recognition ability of the proposed biosensor based on TDN probe is one order of magnitude stronger than that of ssDNA. Owing to its desirable merits of label-free, ultra-sensitivity, low LoD and compact size (with length of 3 mm), the proposed OFB reveals the DNA molecular conformational and dynamic processes evolutions, which can construct an innovative in vitro detection platform and find broad potential for applications in the life and chemical sciences.

Acknowledgements

This work was supported by the Natural Science Foundation of the Jiangsu Higher Education Institutions of China (Grant Nos. 25KJB416001 and 22KJB510034), the National Natural Science Foundation of China (Grant Nos. 12174199 and 11704199), the Scientific Research Foundation for High-level Talents in Nanjing Vocational College of Information Technology (Grant No. YB202410), the China Postdoctoral Science Foundation (Grant No. 2021M701765), General Program of Natural Science Foundation of Jiangsu Province (Grant No. BK20221330), Jiangsu University 'Blue Project' Funding, Postgraduate Research & Practice Innovation Programs of Jiangsu Province, and Jiangsu Province Higher Education Teaching Reform Research Project (Grant No. 2025JGYB487).

References

[1] Gilboa T, Garden P M and Cohen L 2020 *Anal. Chim. Acta* **61** 1115
[2] Wang C H, Zhang Y, Huang T W and Yang Z C 2024 *IEEE Trans. Netw. Sci. Eng.* **11** 6550
[3] Zhang H Y and Miller B L 2019 *Biosens. Bioelectron.* **141** 111476
[4] Ribeiro B V, Cordeiro T A R, Freitas G R O, Ferreira L F and Franco D L 2020 *Talanta Open* **2** 100007
[5] Kong J W, Dou S X, Li W, Li H and Wang P Y 2023 *Chin. Phys. Lett.* **40** 078701
[6] Zhao S Q, Jia Y X, Wang A P and Yang L 2023 *Biosens. Bioelectron.* **239** 115613
[7] Fan Z Q, Yao B, Ding Y D, Zhao J and Xie M H 2021 *Biosens. Bioelectron.* **178** 113015
[8] Li Z, Yi Y, Luo X, *et al*. 2020 *J. med. virol.* **92** 1518
[9] Shaimerdenova M, Ayupova T, Ashikbayeva Z, Bekmurzayeva A, Blanc W and Tosi D 2023 *J. Lightwave Technol.* **41** 4114

[10] Saha U, Madaboosi N, Sai V V R and Bandyopadhyay S 2024 *IEEE Sens. Lett.* **8** 5000104
[11] Wu T, Ding L Y, Zhang Y M and Fang Wu 2022 *IEEE Sens. J.* **22** 12485
[12] Lang X Z, Singh R, Zhang B Y and Kumar S 2024 *IEEE Sens. J.* **24** 1564
[13] Delgado-Pinar M, Shi Q, Poveda-Wong L, *et al*. 2017 *IEEE Sens. J.* **17** 5503
[14] Li X S, Singh R, Zhang B Y, *et al*. 2024 *IEEE Sens. J.* **24** 4480
[15] Wan H D, Chen X Y, Zhang S T, Xiong J X, Jiang W F, Liu H Z, Wan C, Wang J L, Xiao Y, Wu Z J and Chao J 2024 *Opt. Express* **32** 31514
[16] Cao H Y, Wei D D, Hu Y Y, Liu B, Fu Y and Liu J 2024 *IEEE Sens. J.* **24** 31735
[17] Gong P Q, Li X G, Zhao Q M, Zhou X, Zhang Y N and Zhao Y 2024 *Opt. Laser Technol.* **168** 109978
[18] Wen H Y, Huang C W, Li Y L, *et al*. 2020 *Sensors* **20** 1509
[19] Li Y P, Fang F, Yang L Y, Tan S J, Yan Z J and Sun Q Z 2020 *Opt. Express* **28** 970
[20] Li L L, Yu S, Jing C L, Chen L H and Zhou A 2024 *IEEE Sens. J.* **24** 17387
[21] Ran Y, Xu Z Y, Chen M F, Guan B O, *et al*. 2022 *Advanced Science* **9** 2200456
[22] Li H T, Wang X, Wu H, *et al*. 2024 *Biosens. Bioelectron.* **264** 116672
[23] Huang T Q, Lu L, Wang H Z, *et al*. 2022 *ACS Sens.* **7** 1926
[24] Yuan H, Yang Y, *et al*. 2023 *Anal. Chem.* **95** 5142
[25] Wang L and Chong L 2025 *RSC adv.* **15** 1831
[26] Feng D Z, Su J, Xu Y, He G F, Wan C G, Wang X, Pan T R, Ding X T and Mi X Q 2021 *Microsyst. Nanoeng.* **7** 33
[27] Mitchell N, Schlapak R, Kastner M, Armitage D, *et al*. 2009 *Angew. Chem. Int. Ed.* **48** 525
[28] Su J S, Liu T S, Wang M, Xu W S, Liu J L, Lan J N, Chen Y J, Xu H, Guo D H and Lai Z M 2025 *Anal. Chim. Acta* **1334** 343419
[29] Ding M, Wang P and Brambilla G 2012 *Opt. Express* **20** 5402
[30] Yang F, Li Q, Wang L H, Zhang G J, Fan C H, *et al*. 2018 *ACS Sens.* **3** 903
[31] Lin M H, Song P, Zhou G B, Fan C H, *et al*. 2016 *Nat. Protoc.* **11** 1244
[32] Chen W J, Özdemir Ş K, Zhao G M, Wiersig J and Yang L 2017 *Nature* **548** 192
[33] Yang Q C, Xu Z Y, Long J Q, Wang H P, Ran Y and Guan B O 2025 *Nat. Commun.* **16** 6250
[34] Wang Y J, Zhang H, Duan S X, Lin W, Liu B and Wu J X 2021 *IEEE Sens. J.* **21** 9148
[35] Suhailin F H, Alwahib A A and Chee H Y 2022 *IEEE Sens. J.* **22** 20516
[36] Yin Z Y, Zhang Z B and Jing X L 2025 *Anal. Chim. Acta* **1333** 343385
[37] Zhou X, Hui Y P and Chen Z X 2024 *Opt. Laser Technol.* **177** 111187
[38] Li X, Zhao Q and Zhang Y 2024 *IEEE Trans. Instrum. Meas.* **73** 7003708